A pattern-based strategy for InSAR phase unwrapping and application to two landslides in Colorado

Yusuf Eshqi Molan[1], and Rowena B. Lohman[1]

[1]Department of Earth and Atmospheric Sciences, Cornell university, Ithaca, NY, US

Corresponding author: Yusuf Eshqi Molan (yeshqimolan@smu.edu)

Key Points:

- Here we use a pattern-based approach for phase unwrapping of InSAR observations of fast-moving landslides.
- We define a similarity index and an error function to determine the most similar unwrapped phase to a scaled reference displacement map.
- We show that our approach can be used for time spans well beyond those where traditional phase unwrapping performs well.

Abstract

Interferometric synthetic aperture radar (InSAR) has been successfully used to map ground displacements associate with landslides. One challenge with InSAR is that the basic measurement of interferometric phase takes values between 0 and 2π instead of values representing total displacement relative to some stable reference frame. Phase unwrapping is necessary to reconstruct measurements of total displacement for use in quantitative analysis. Unwrapping approaches often assume that the absolute phase difference between two neighboring pixels should be a small fraction of a cycle (π or less). In the presence of noise or high strain rates associated with fast-moving landslides, aliasing of the phase (under-sampling of the wrapped signal) can result in unwrapping errors and under- or overestimates of total displacement. Here we use a pattern-based strategy for phase unwrapping of InSAR observations of fast-moving landslides, where we determine the unwrapped deformation field that is most similar to a scaled reference displacement map. We also describe a range of metrics that we use to evaluate the most appropriate scaling for each interferogram and demonstrate the range of conditions where they perform well using synthetic data. For evaluation of the results, we generated UAVSAR wrapped interferograms over the Slumgullion landslide in Colorado where phase aliasing for interferograms with temporal baselines larger than seven days is common. We show the interferograms unwrapped with our approach and compare them against results from range offsets (pixel tracking), demonstrating that our approach can be used for time spans well beyond those where traditional phase unwrapping performs well.

Plain Language Summary

InSAR allows measurement of surface displacement due to earthquakes, landslides, and many other factors. However, InSAR requires a step known as "unwrapping" to convert the raw observations into quantitative measurements of displacement. Most unwrapping methods assume some degree of spatial and/or temporal continuity within the signal. In the presence of high strain rates, such as those observed on fast-moving landslides, these unwrapping approaches are not reliable. We use a pattern-based strategy for InSAR phase unwrapping that seeks the final model that best fits a scaled initial estimate of the deformation signal. We demonstrate this approach using synthetic data and UAVSAR observations over the Slumgullion landslide in Colorado, which has a displacement rate of up to 2 cm/day. With such a fast displacement rate, InSAR observations that span more than 7 days contain so much deformation that traditional unwrapping approaches almost always fail. We show that our approach can reliably unwrap interferograms spanning much larger time intervals, and validate these results with independent measures of the displacement between each pair of images.

1. Introduction

Landslides and other forms of mass wastage are some of the most devastating processes shaping the modern landscape, and present significant hazards to populations and human structures that lie in their path. Landslide movement is regulated by a wide range of environmental and geological factors (e.g., Wang et al., 2018; Handwerger et al., 2019; Handwerger et al., 2019; Shi et al., 2019), which combine to make predicting their behavior very challenging (Iverson et al., 2000). Their unpredictability makes landslides one of the most dangerous geo-hazards (e.g., Kirschbaum & Stanley, 2018; Kirschbaum et al., 2015; Froude & Petley, 2018); they are often the cause of human casualties and injuries, disruption of transportation and communication networks, destruction of property and other economic and

social costs (e.g., Oven, 2009). Recent studies suggest that landslide-related hazards are worsening, due to a combination of climate change and population growth in areas that are impacted by landslides (e.g., Froude & Petley, 2018; Gariano & Guzzetti, 2016). Earthquakes, severe rainfall, and anthropogenic or natural changes in vegetation are all factors that can contribute to changes in the rate of movement or catastrophic failure of a previously inactive or slow-moving landslide.

One of the most basic tools for understanding and forecasting landslide behavior is the measurement of displacement rates and their variability over time (e.g., Wasowski & Bovenga, 2014; Bekaert et al., 2020). Interferometric Synthetic Aperture Radar (InSAR), which has a spatial resolution of tens of meters or better, provides an all-weather, day-or-night capability to generate mm–cm scale displacement time-series under a range of different climate and geomorphologic regimes (e.g., Bürgmann et al., 2000; Rosen et al., 2000). SAR images have wide spatial coverage, with a swath width of tens to hundreds of kilometers (e.g., Lu & Dzurisin, 2014), and can achieve sub-weekly repeat times, including repeat observations as frequently as every 6-days for the free and open data from the Sentinel-1a/b constellation. InSAR has been successfully used to detect surface deformation due to various mechanisms, such as volcanism (e.g., Lu & Dzurisin, 2014), subsidence (e.g., Qu et al., 2015), permafrost (e.g., Molan et al., 2018), earthquakes (e.g., Lohman & Barnhart, 2010; Scott & Lohman, 2016) and landslides exhibiting a range of behaviors and rates of motion (e.g., Wasowski & Bovenga, 2014; Bekaert et al., 2020; Hu et al., 2020).

One challenge facing InSAR users stems from a limitation inherent to the data itself. The basic observation in InSAR is of the change in travel time between the ground and the satellite, but this observation is only made to within a fraction of a wavelength, rather than in the absolute number of cycles traveled by the radar signal. This measurement of InSAR phase is often described as being "wrapped" to the fraction of 2π radians in each cycle; there is always an ambiguity in terms of the total change in distance. Even within a single interferogram, deformation and atmospheric noise can contribute more than one cycle of travel time change, resulting in ambiguities even in the strain present between any two points within the image. Therefore, unwrapping, or a model of the 2π transitions that would result in a physically reasonable deformation field, is necessary. Unwrapping is a mathematically ill-posed problem and, particularly in the presence of high strain rates or larger amounts of noise, can have more than one solution. Aliasing of the phase (i.e., undersampling of the wrapped signal) in deforming regions is particularly problematic when the displacement between two adjacent pixels within the interferogram is large relative to the wavelength of the radar (e.g., Itoh, 1982; Ghiglia & Pritt, 1998; Yu et al., 2019). This problem can occur either when the displacement rates are high, as in a fast-moving landslide, or when the time between high-quality acquisitions is long, which can occur in areas with seasonal snow cover or for satellites with infrequent observations. Even when the deformation signal is not formally undersampled, the presence of noise in high-strain regions can introduce ambiguities in terms of the appropriate choice of phase unwrapping.

Several unwrapping approaches have been introduced to find the solution for the unwrapping problem (e.g., Chen & Zebker, 2011; Costantini, 1998). Phase unwrapping is often performed entirely in the spatial domain, on individual interferograms, and usually involves the assumption that the absolute phase difference between two neighboring pixels should be small, usually smaller than π (e.g., Itoh, 1982; Ghiglia & Pritt, 1998; Yu et al., 2019). As mentioned above, for fast-moving landslides there may be large numbers of phase discontinuities within the

deforming region, even for interferograms spanning short time intervals. In such cases, unwrapping approaches that assume spatial continuity may not perform well (e.g., Manconi, 2021; Hu et al., 2020). For example, almost all UAVSAR interferograms over Slumgullion landslide in Colorado with baselines greater than 7 days suffer from phase aliasing and are not used in studies of that slide (Hu et al., 2020).

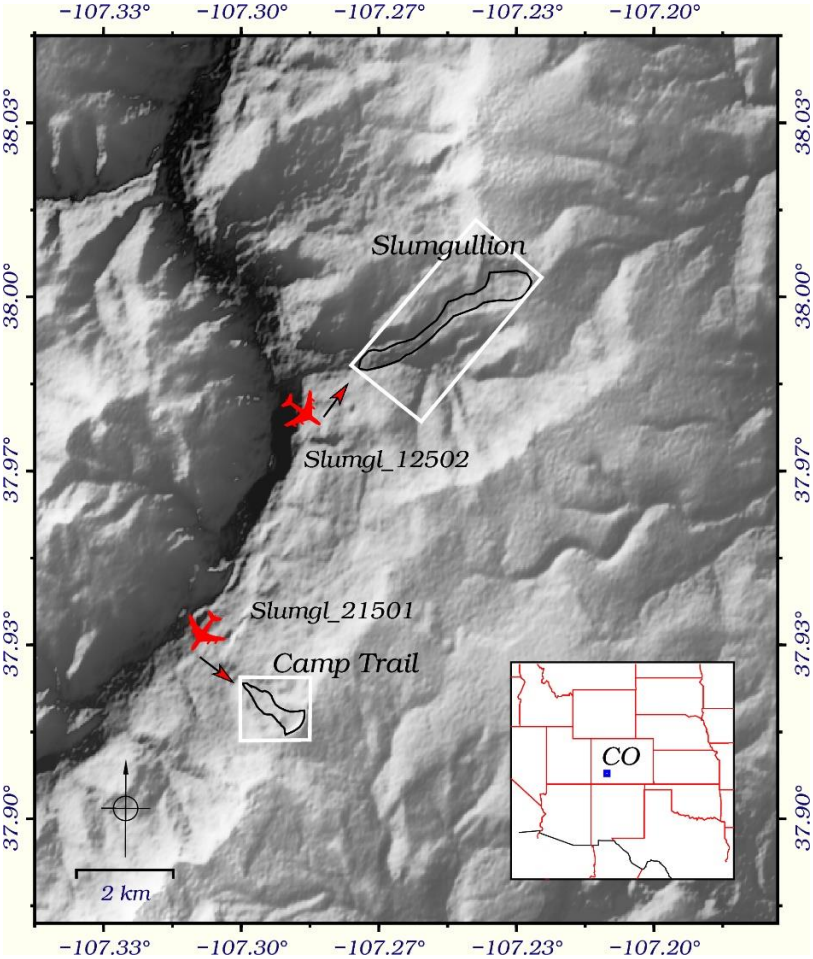

Figure 1. Location of UAVSAR tracks 12502 and 21501 within the study area (location shown in inset), with flight path and viewing direction (red symbols and arrows) and outline of the Slumgullion and Camp Trail landslides (black lines). The study areas are shown in white. Figure was generated using the pyGMT package (Wessel et al., 2019; Uieda et al., 2021).

Here, we develop a pattern-based strategy for unwrapping interferometric phase over landslides where current unwrapping methods fail due to fast displacement rates. We apply our approach to a set of UAVSAR interferograms covering a landslide in southeastern Colorado, here referred to as the Camp Trail landslide (Figure 1, sample interferograms shown in Figure 2). The two landslides, Camp Trail and Slumgullion landslides, are located in the San Juan Mountains, southwestern Colorado, USA (Lipman, 1976). The Camp Trail landslide, which is introduced for the first time in this paper and is named after a trail that passes the landslide (USGS, 2016), is located 12 km south of the well-studied Slumgullion landslide (e.g., Wang et al., 2018; Hu et al., 2020). We demonstrate the performance of our algorithm on a set of

synthetic interferograms generated using displacement rates similar to those found in the real data. We also show the results of our approach on UAVSAR interferograms over both of the landslides.

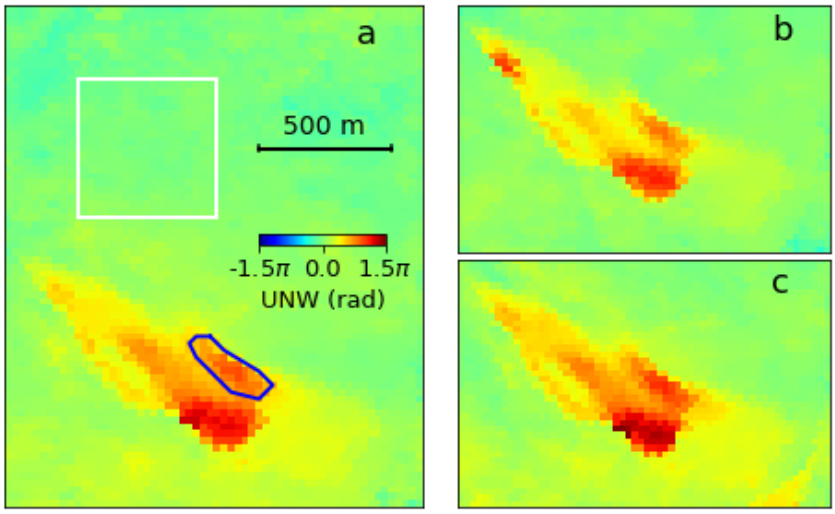

Figure 2. a) Unwrapped phase in radians (UNW) for the reference interferogram covering the Camp Trail landslide (20180802-20181003). b), and c) are interferograms spanning 20170905-20171025, and 20180725-20181003, respectively. Location of panels (b) and (c) is shown in Figure 1, (a) extends slightly to the north. The reference area is boxed in white, and the subsection used in our synthetic scenarios is outlined in dark blue. All the interferograms are shown in the same color scale (-1.5π – 1.5π).

In the following, we define our unwrapping approach in Section 2. We generate synthetic interferograms with predefined displacement rates to demonstrate the feasibility of our method in Section 3. Then, in Section 4, we evaluate our method using real interferograms covering the Slumgullion landslide. We investigate the temporal behavior of the Slumgullion landslide, using a combination of longer-timescale interferograms and range-offset pixel tracking. In Section 5, we present our conclusions and discuss the relevance of this work to other regions.

2. Methods

2.1 Phase unwrapping

As described above, transforming the original, modulo-2π interferometric phase into a physically meaningful map of deformation requires the process of phase unwrapping. Several approaches have been introduced to find the solution for the unwrapping problem. Unwrapping algorithms based on single interferograms (i.e., 2-D unwrapping approaches) can generally be divided into two main categories: path following, and optimization-based methods. The assumption in the path following methods is that the Itoh condition (the requirement that the correctly unwrapped phase difference between two adjacent pixels is less than π) is met along the integration path (e.g., Ghiglia & Pritt, 1998; Madsen et al., 1993; Xu & Cumming, 1999; Flynn, 1997). One example of this methods is Goldstein's branch-cut algorithm (Goldstein et al., 1988).

The optimization-based methods rely on objective functions that have characteristics similar to those we expect to see in realistic unwrapped interferograms (e.g., Yu et al., 2013; Dias & Leitao, 2002). This category includes statistics-based methods and L-p norm methods. The L-p norm methods minimize the difference between gradients in the unwrapped phase and wrapped phase gradients. This category includes least square (LS) (Fried, 1977), and minimum cost flow (MCF) (Costantini, 1998), respectively for p=2, and p=1. The statistics-based methods attempt to maximize the conditional probability of the phase unwrapping results, often by placing constraints on how spatially smooth the final unwrapped solution should be (e.g., Yu et al., 2019). The SNAPHU software package (Chen & Zebker, 2011) is one of the most frequently used implementations of these statistics-based methods.

Other phase unwrapping approaches take advantage of assumptions that can be made about deformation behavior over time. These assumptions are often based on the existence of an InSAR time series instead of single interferograms. So far, several unwrapping methods of this sort, sometimes referred to as "3D" unwrapping methods, have been introduced (e.g., Costantini et al., 2002; Pepe & Lanari, 2006; Hooper & Zebker, 2007; Pepe et al., 2011; Fornaro et al., 2011; Devanthéry et al., 2014). These approaches generally require that the unwrapped phase be as close as possible to a model of deformation behavior that varies smoothly over time or is even constant (e.g., Mora et al., 2003; Goel & Adam, 2014; Perissin & Wang, 2012; Crosetto et al., 2008; Ferretti et al., 2001). The assumption of a constant, or even a smoothly varying displacement history, however, can potentially cause significant unwrapping errors in locations where the actual deformation varies significantly in time (e.g., Crosetto et al., 2016).

2.2 Pattern-based phase unwrapping

Studies of fast-moving landslides face many of the challenges described above. The spatial continuity which is the core assumption in 2-D unwrapping methods is often not preserved at landslide boundaries where non-moving pixels outside of the landslide can be immediately adjacent to rapidly moving pixels. The same condition can also happen at the boundary between two landslide subsections moving at different rates. These high strain rates and discontinuities can result in phase jumps between pixels that violate the Itoh condition and make it impossible for 2-D approaches to resolve the 2π ambiguities present in the wrapped interferograms. Similarly, 3D unwrapping approaches are hampered by the temporal variability of behavior within landslides, which is often closely related to rainfall and freeze/thaw conditions, or to triggering events such as earthquakes or anthropogenic activity (e.g., Handwerger et al., 2019; Chen et al., 2017; Carrière et al., 2018; Huang et al., 2017; Schulz & Wang, 2014; Petley et al., 2007). We demonstrate an approach for addressing the unwrapping problem associated with fast-moving landslides through a requirement that the pattern of deformation, but not the magnitude, be as similar as possible within a set of unwrapped interferograms. This can be viewed as an extension of the 3D approaches that use a constant displacement rate model, with the addition that we also solve for the best-fit scaling term for that model for each interferogram.

The wrapped phase, w_i, at a given pixel, i is related to the correctly unwrapped phase, u_i^{true} as:

$$u_i^{true} = 2\pi c_i^{true} + w_i \quad (1)$$

where c_i^{true} is the actual number of cycles between the unwrapped and wrapped phase, in reference to some region within the interferogram that is defined as zero. In the examples below,

we define a 40 × 40 (pixels) window in a stable area close to the landslide as our reference (see Figure 2). The estimated unwrapped phase is:

$$u_i = 2\pi c_i + w_i \quad (2)$$

where, for the 3D approaches that use a constant displacement rate model, c_i is an integer chosen to minimize the difference between the unwrapped phase and a displacement rate, v_i, scaled by the timespan of the interferogram, t:

$$c_i = round(\frac{tv_i - w_i}{2\pi}) \quad (3)$$

This strategy can be used only when the expected displacement rate for each pixel can be inferred, either from an average over a subset of the interferograms or from the set of data as a whole, and where this rate remains fairly constant over time. However, the behavior of landslides can be complex and time-varying, with potentially very short-lived precursors and transients. Generally, landslides move faster in summer and slower in winter (e.g., Delbridge et al., 2016). The rate and style of deformation can change significantly for different years depending on the amount of precipitation and recharge. Therefore, the average displacement rate may not serve as an appropriate metric to use in phase unwrapping of a given interferogram. However, for some landslides, there may be similarities in the style of deformation between different regions over time, even when the landslide as a whole is moving more rapidly or slowly than on average. To explore this, we add a "scaling factor" to Equation 3 to account for the accelerations and decelerations that occur during the time series. Instead of the predicted displacement for a given interferogram with timespan t being tv_i, we also solve for a scaling factor, R, that is constant over the entire area of interest (landslide) during each interferogram. This approach assumes that a given region of the landslide that moves faster than other portions would tend to move even faster if the landslide as a whole accelerates, and would continue to move more quickly than slow regions during time periods where the landslide exhibited little deformation. Under this formulation, the choice of c_i becomes an equation for two unknowns, v_i, which varies from pixel to pixel, and R, which is a constant over the entire area of the landslide:

$$c_i = round(\frac{Rtv_i - w_i}{2\pi}) \quad (4)$$

making the final unwrapped interferogram:

$$u_i = 2\pi\, round\left(\frac{RTv_i - w_i}{2\pi}\right) + w_i \quad (5)$$

The above analysis contains two unknowns, v_i and R. We resolve the first unknown, v_i, by assigning this value based on one or more unwrapped interferograms with short timespans, for which we have confidence in the phase unwrapping. In the examples below, we explore the robustness of this assumption through the use of synthetic data. We also have tested our approach using a range of difference short-timescale interferograms and found no major impact on the final unwrapped longer-timescale interferograms.

We examine two methods for determining the appropriate scaling value, R, for each interferogram. Both are based on different measures of the size of the residual between the unwrapped data and the scaled reference velocity:

$$u_i^{res} = u_i - Rtv_i \quad (7)$$

u_i^{res} contains the impact of true variations in strain behavior within the slide (i.e., a region that moves more quickly relative to other regions than it does in the reference interferogram) as well as noise within the data and errors in the unwrapping. For instance, when the value of R is much

too low or too high, there will be many unwrapping errors relative to the case where the value of R is chosen appropriately. The nonlinearity in equation (4) and the spatial variability of the reference displacement rate, v_i, impact how u_i^{res} varies across the landslide for a given value of R. By definition, the values of u_i can only differ from the wrapped values, w_i, by quantiles of 2π, but the values of R where the 2π jumps occur will differ from pixel to pixel, unless v_i is a constant across the entire landslide (in which case, this approach would neither work, nor be necessary). The optimal value of R will result in a predicted displacement field, Rtv_i that is most similar to the correctly unwrapped phase. Our first metric is based on the root-mean-squared error (RMSE) of the real-valued unwrapped residual in Equation 7:

$$RMSE = \sqrt{\frac{\sum_{i=1}^{n}\left(u_i^{res}\right)^2}{n}} \tag{8}$$

Values of R that result in poorly-unwrapped outcomes will contain short-spatial-scale discontinuities that differ from the predicted displacement field and result in larger values of RMSE. In cases where the data has low levels of noise and the actual deformation during that time interval is similar in character to a scaled version of v_i, this approach should result in the correct unwrapping, such that $c_i \sim c_i^{true}$ and $u_i \sim tv_i^{true} = u_i^{true}$. However, for noisier data, or time periods where the pattern of strain within the landslide differs significantly from the pattern present during the reference time periods, this approach will not be reliable.

The second metric is based on the size of the residual term within the complex domain, which we refer to as the displacement pattern similarity index (DPSI):

$$DPSI = \left|\sum_{i=1}^{n} e^{ju_i}\left(e^{jRtv_i}\right)^*\right| \tag{9}$$

The similarity function, *DPSI*, takes positive values between zero and one indicating no similarity and full similarity.

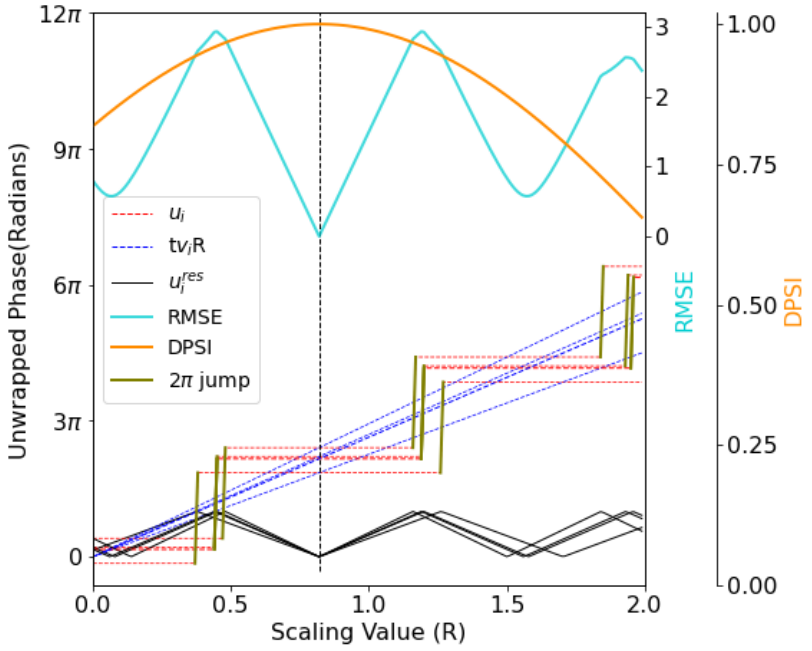

Figure 3. RMSE (solid cyan line) and DPSI (solid orange line) for simplified four-pixel synthetic scenario with u_i^{res}=0. The vertical olive lines are the location of 2π jumps which corresponds to the value of R where the ambiguity number c_i jumps to a higher value for that pixel. Black solid lines indicate the

difference between the unwrapped interferogram (red dashed line) and scaled displacement rate, Rtv_i (blue dashed line) for each pixel and value of R. Note that the peak value of DPSI and the minimum value of RMSE agree, and that RMSE has secondary, broader minima as well.

Figure 3 illustrates these quantities for a simplified scenario involving only four pixels, where the displacement, $u_i^{true} = 0.82\ tv_i$. For this scenario, we add no noise, so *RMSE* = 0 at the correct value of *R=0.82*. v_i is different at each pixel, as would be expected for a real-world scenario. Figure 3 shows the scaled deformation rate for each pixel, Rtv_i (blue dashed line), unwrapped values for the four pixels (red dashed lines, 2π jumps shown in olive), and the residual, u_i^{res} (black lines) for each value of *R* between 0 and 2. Note how each pixel has multiple minima where $u_i^{res} = 0$, but that the positions of these minima vary except for the one at the correct value of *R=0.82*. RMSE and DPSI both have their minima and maxima at the correct value, respectively. As the number of pixels used, *n*, increases, the secondary minima in RMSE will decrease in importance.

3. Synthetic tests

3.1 Synthetic interferograms for Camp Trail landslide, including noise

Here, we extend the simple scenario which is shown in Figure 3 to include noise, a larger number of points, and variations in *v* over time. Figure 2 shows three unwrapped interferograms from track T21501 covering the Camp Trail landslide (location in Figure 1). We select the interferogram 20180802-20181003 (61-day temporal baseline) as the reference interferogram that we use in our synthetic tests. Then, we generate synthetic unwrapped interferograms and define v_i based on the reference interferogram.

$$u_i^{syn} = tv_i R_0 + n_i \tag{10}$$

where here we use *t*=305 days (5 times the reference time interval) and R_0 = 0.75, and add normally distributed noise, n_i, with a range of values for the standard deviation, σ. We then wrap the synthetic interferograms onto the interval $[-\pi, +\pi]$ to generate the synthetic wrapped interferogram values, w_i^{syn} and then solve for the estimated unwrapped phase, u_i for each value of R. In Figure 4, we use n_i with σ = 1.0 radian and show the resulting unwrapped values and RMSE/DPSI for a range of *R*. We also show how the results of this synthetic scenario vary for σ = 0.0, 0.75 and 1.5 radians (Figure 5). In Figure 5, we only show the phase jumps of individual pixels, not their unwrapped values, for clarity. Figure 5 also shows the associated corrected unwrapped interferograms.

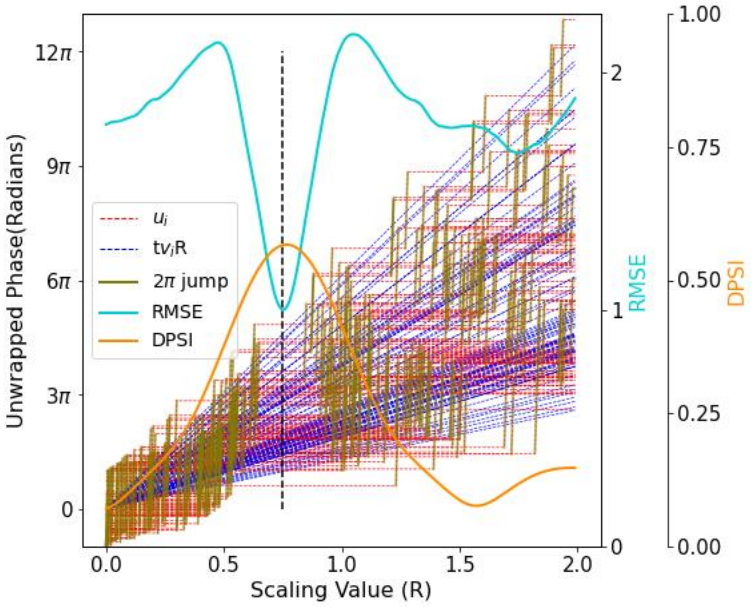

Figure 4. Camp Trail synthetic scenario, symbols as in Figure 3. Only 20% of the pixels are shown, for clarity.

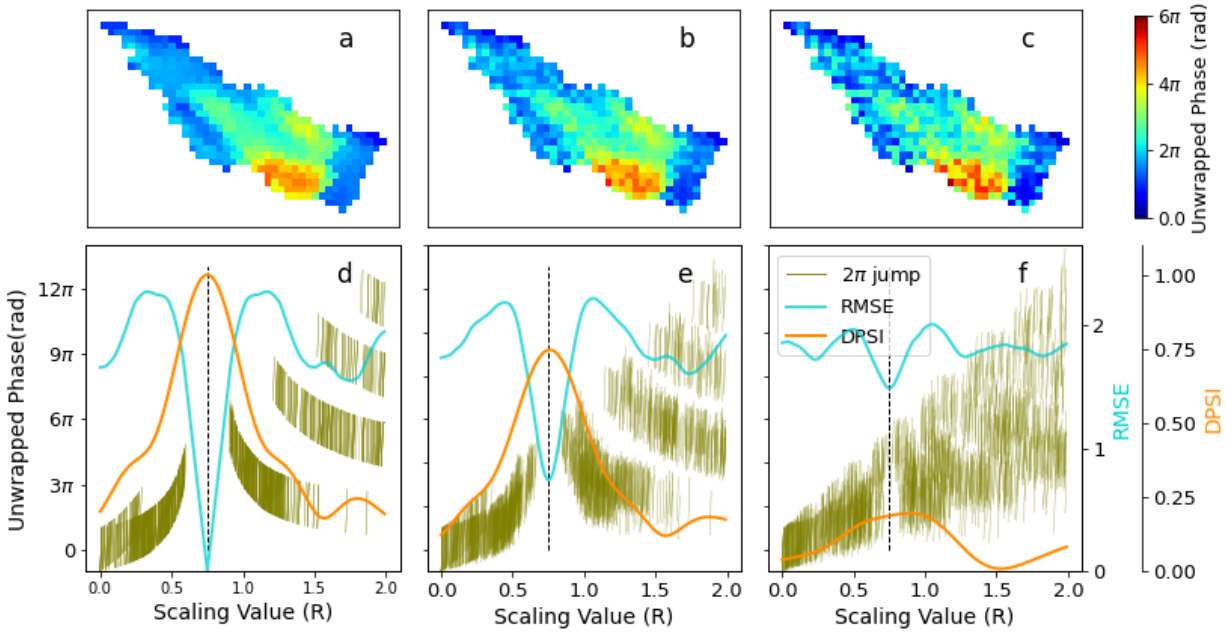

Figure 5. The synthetic unwrapped interferograms generated using normally distributed random errors with the standard deviations of 0.0, 0.75, and 1.5 radians illustrated in a, b, and c, respectively. RMSE and DPSI plots for the three synthetic interferograms are shown, respectively, in d, e, and f.

The examples shown in both Figures 3 and 4 show that the correct value of $R=R_0$ can be found using either the *RMSE* or *DPSI* metric, although the sensitivity to the correct value is

much lower for the noisiest example considered here. However, even the correct value of $R=R_0$ will result in incorrectly unwrapped pixels, to a degree that increases with the level of noise.

Figure 6 illustrates how the estimated value of R and the percentage of incorrectly unwrapped pixels changes as the level of noise increases. We show the result of increasing the value of σ for different levels from 0 to 2 radians with the interval of 0.1 radians. For each level of σ, 201 random realizations of the data set were generated. Then, for each random set, RMSE, DPSI, R, and the percentage of incorrectly unwrapped pixels were calculated. Both metrics perform well up to a noise level of around σ=1.2 radians, above which the DPSI metric starts to diverge from the correct value of R and leads to a higher percentage of incorrectly unwrapped pixels. The RMSE metric estimates the correct scaling value and leads to a negligible number of incorrectly unwrapped pixels below σ=1.65. Above a value of around 1.65 radians for the standard deviation of the noise σ, the percentage of incorrectly unwrapped pixels using the RMSE metric increases rapidly.

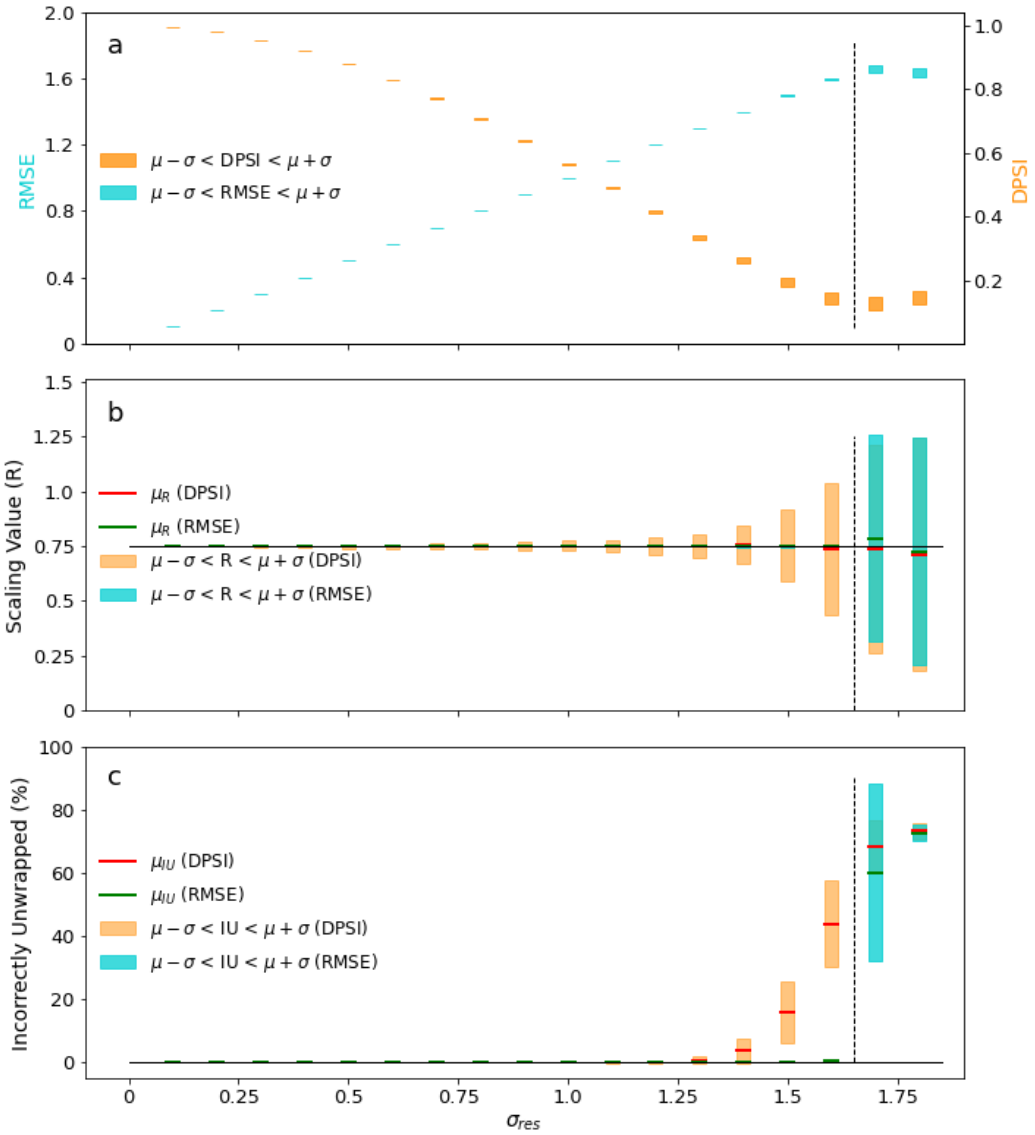

Figure 6. a) RMSE and DPSI plotted for different level of noise. The black vertical dashed line marks σ=1.65. The plots of inferred scaling value and incorrectly unwrapped pixels are illustrated in b and c, respectively. The black horizontal solid lines in (b) and (c) mark the true scaling value (0.75) and zero incorrectly unwrapped pixels.

3.2 Synthetic interferograms for Camp Trail Landslide: Sub-sections with different behaviors

A deforming region such as a landslide can contain sub-regions that accelerate and decelerate at different rates (e.g., Delbridge et al., 2016). To examine the impact of temporal complexity, we generate synthetic interferograms for the Camp Trail scenario that contain a smaller sub-section of the slide with a 20% higher value of the actual scaling values, R_0. Figure 2a shows the reference interferogram we used and the boundary of the subsection (R_0=0.88), which has a 20% higher actual scaling value, R_0 than the rest of the landslide (R_0=0.72). The average value of R_0 across the entire area of the landslide is 0.75.

We calculated *RMSE*, *DPSI*, *R*, and the percentage of incorrectly unwrapped pixels for different levels of σ from 0 to 2 radians with the interval of 0.1 radians in the same manner as in Section 3.1 (Appendix A, Figure A-1). Just as seen in the example explored in Section 3.1, the error function *RMSE* is successful in estimating the correct average value of scaling, *R*, and results in very small (<1%) percentages of incorrectly wrapped pixels when the noise is generated with standard deviation values smaller than about 1.65 radians. As expected, the number of incorrectly wrapped pixels is larger than for the case where the data was generated using a constant value of R_0. The *DPSI* metric begins to diverge from the correct solution for noise generated with standard deviation values larger than about 1.2 radians. The plots of estimated scaling values and incorrectly unwrapped phases in Figures 6, and A-1 show that the number of mismatched pixels, *i.e.*, unwrapping errors, increases drastically for both data sets when the standard deviation of residual phase becomes greater than 1.65 radian. Also, at the standard deviation higher than 1.65, *DPSI* decreases to smaller than 0.15 values. Therefore, *RMSE*=1.65 and *DPSI*=0.15 (equivalent to σ≈ 1.65) can be considered as the threshold to distinguish correctly unwrapped images, at least for scenarios similar in spatial scale and strain rates as those explored here.

4. Evaluation using real data

We used UAVSAR data over the Slumgullion landslide to evaluate our pattern-based unwrapping approach. Remote sensing studies and in-situ measurements suggest that the Slumgullion landslide is characterized by rapid deformation with rates of up to 2 cm/day (e.g., Delbridge et al., 2016; Coe et al., 2003). Much of the motion appears to occur during the spring and summer, suggesting that variations in pore pressure associated with precipitation and snow melt may play a large role in controlling the amount of deformation (e.g., Delbridge et al., 2016; Coe et al., 2003). The active slide is about 300 m wide and 4 km long, with a front to toe elevation difference of about 540 m (e.g., Coe et al., 2003; Mohlenbrock, 1989; Gomberg et al., 1995). InSAR has been successfully used to measure the spatial and temporal behavior of some creeping landslides, including Slumgullion (e.g., Bekaert et al., 2020; Hu et al., 2019; Handwerger et al., 2013). However, the rapid, several cm/day displacement rate of the Slumgullion landslide results in aliasing and loss of coherence for most UAVSAR

interferograms covering timespans longer than a week and limits the time periods that can be studied using this data and traditional unwrapping approaches.

One strategy that has been successfully used to map deformation in fast-moving landslides is the tracking of pixel offsets in both optical and SAR imagery. Various offset tracking methods have been developed so far and applied to deformation mapping and monitoring (e.g., Le Bivic et al., 2017; Raspini et al., 2015). The advantages of offset tracking compared to use of the InSAR technique are that offset tracking is not influenced by the need for phase unwrapping and difficulties with aliasing, and the need for a reference point or region is reduced. Tracking of pixel offsets provides measurements in both the azimuth and range directions, unlike InSAR, which only provides a measurement in the range direction unless split-beam or multiple-aperture interferometry methods are used (e.g., Bechor & Zebker, 2006; Grandin et al., 2016). However, when correctly unwrapped, InSAR provides a more precise measurement of deformation in the range direction when compared to offset tracking. The azimuth and range offset accuracies are estimated to be on the order of 1/16, and 1/32 of the ground pixel spacing dimensions, respectively (e.g., Casu et al., 2011; Singleton et al., 2014; Sun & Muller, 2016). In the range direction, using UAVSAR data with range pixel size of 1.67 m, the accuracy of range offsets tracking is expected to be about 5 cm. Considering that the displacement rate of the Slumgullion landslide is 1-2 cm/day, this level of accuracy is a small fraction of total displacement occurring between pairs of images spanning several weeks or more, so useful measurements of displacements in the range direction can be provided by offset tracking over those time spans. However, for shorter time-scale pairs, the noise in the offset-tracking results is expected to be larger than the actual ground displacement signal.

We used thirty-four HH polarized UAVSAR single look complex (SLC) images acquired from path 12502 between Aug. 11, 2011, and July 19, 2019, to generate seventy-six interferograms spanning time intervals of up to 9.5 months. We downloaded data from NASA's UAVSAR data website (https://uavsar.jpl.nasa.gov/). We processed the interferograms using the ISCE-2 software (Agram et al., 2016). We removed the impact of topography with (put in name of DEM and reference here). We multi-looked the interferograms by 6 and 17 in the range and azimuth directions, respectively. Because the original resolution of the UAVSAR data is 0.6 and 1.67 m in azimuth and range directions, respectively, this is equivalent to pixel sizes of about 10 meters. We performed an initial unwrapping attempt using the Snaphu-Minimum Cost Flow method (Snaphu-MCF, (Chen & Zebker, 2002)). We also generated pixel offsets in the range direction based on UAVSAR single-looked amplitude images using AMPCOR, the pixel offset tracking package embedded in *ISCE-2* software. The reference and the search windows were, respectively 32 × 32 pixels, and 17 × 6 pixels. The correlation oversample factor was 128.

Due to the rapid ground deformation associated with the Slumgullion landslide, all of the interferograms with temporal baselines larger than seven days and even some of the shorter-timescale interferograms included numerous aliasing-induced phase errors after unwrapping using the standard approach described above. Only nine of the unwrapped interferograms, all with temporal baselines of seven days, appear visually to be unaffected by unwrapping errors. We used the average rate of these nine highest-quality interferograms (Figure A-2) as the reference displacement rate (Figure 7). We then used this reference displacement rate to unwrap all the other interferograms (still within range-doppler coordinates to minimize the impact of geo-referencing-related interpolation errors) using our pattern-based method, as described in Section 2

We compare the resulting unwrapped interferograms with pixel offsets in the range direction to evaluate the results and validate our pattern-based unwrapping approach and how it performs over a wide range of timescales and conditions. The range offsets can be compared directly to InSAR phase measurements, which are also in the range direction, but are hampered by the signal to noise constraints discussed above, particularly for short time-scale pairs. Below, we show three examples (dates in Table 2) out of the sixty-eight unwrapped interferograms in our study (Figure 8). Six more examples are shown in Appendix section (Figures A-3 and A-4). Figure 8 shows examples of the interferograms unwrapped using our pattern-based approach, the residual phase u^{res}, and the range direction offsets. We also indicate the inferred value of R for each interferogram. Note that interferogram (c) is associated with a higher value of R (higher rates) than interferogram (b), which overlaps and spans a longer time interval. This suggests some variability in rate over the 133-day time period of (b).

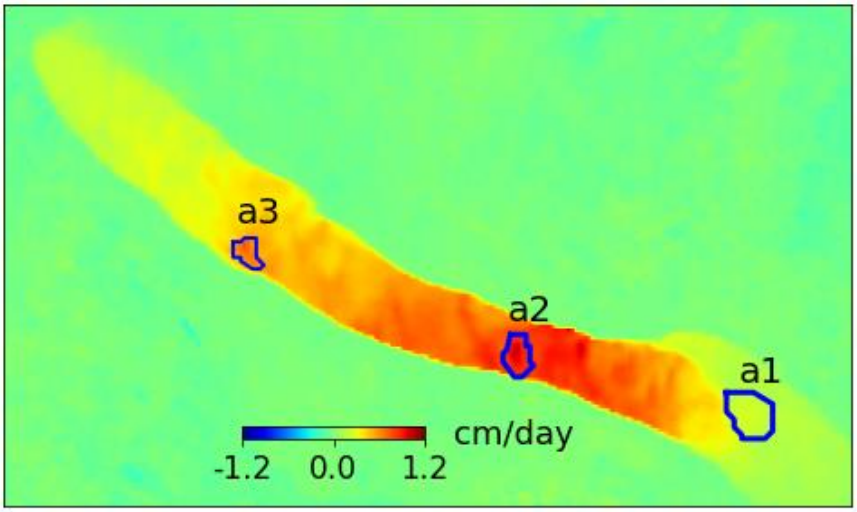

Figure 7. The reference rate and individual regions described in the text. Image shown in range-doppler coordinates, with approximate location and scale indicated in Figure 1.

Table 1. The dates and temporal baselines of the interferograms in Figure 8.

	Interferogram	Temporal Baseline (days)	R	RMSE	DPSI
a	*2018-07-25* *2018-10-03*	70	0.81	1.3	0.46
b	*2016-06-16* *2016-10-27*	133	1.04	1.57	0.39
c	*2019-06-10* *2019-07-15*	35	1.47	1.05	0.80

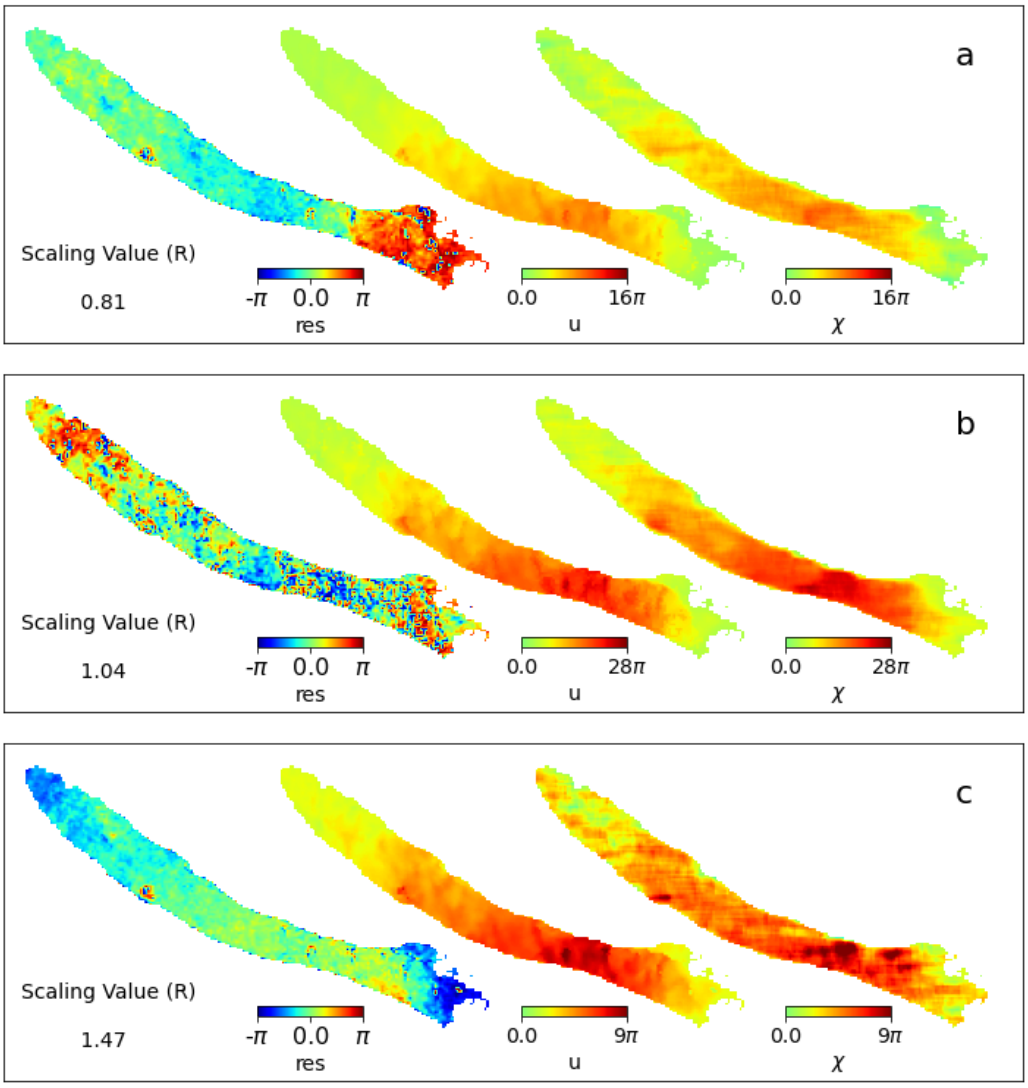

Figure 8. The residual phase, u^{res} (res), unwrapped interferograms (u), and the range direction offsets ($\varkappa$) of interferograms 2018-07-25 to 2018-10-03 (a), 2016-06-16 to 2016-10-27 (b), and 2019-06-10 to 2019-07-15 (c).

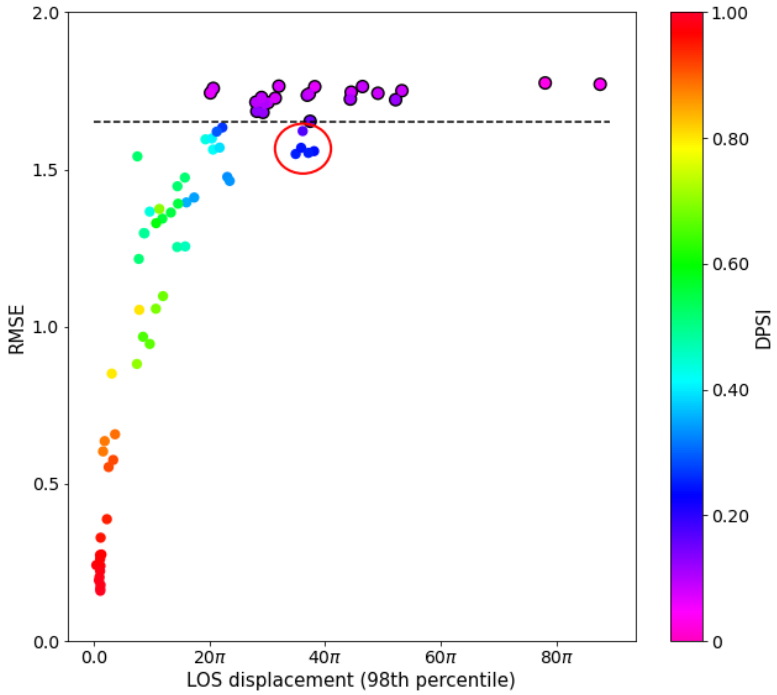

Figure 9. Plot of RMSE and DPSI (color) vs. peak LOS displacement (98th percentile), and RMSE=1.65 cutoff inferred from synthetic tests (black dashed line). Interferograms with DPSI values < 0.15 are also outlined in black. Red circle indicates interferograms unwrapped using a "secondary reference" process described below.

The results of the synthetic data tests described above suggested using *DPSI*=0.15 and *RMSE*=1.65 as the threshold values to identify correctly unwrapped interferograms. Figure 9 illustrates the variations of *RMSE* (y-axis) and DPSI (color) versus the peak displacement (shown as the 98th percentile of LOS displacement of our unwrapped UAVSAR interferograms) over Slumgullion. The black dashed horizontal line on the plot represents *RMSE*=1.65. All the interferogram above the threshold line of RMSE=1.65, or with DPSI values < 0.15 (purple-pink colors) should be considered suspect, according to the synthetic tests. The interferograms with DPSI values smaller than 0.15 are outlined in black in Figure 9 for clarification. The comparison with offset-tracking displacement images showed that all interferograms with RMSE values smaller than 1.65 and DPSI values greater than 0.15 are reliably unwrapped. Some of the interferograms with DPSI and RMSE values outside of these thresholds agree well with the pixel-tracking results and do appear to be correctly unwrapped as well. However, we only consider the forty-five out of sixty-eight interferograms that meet both conditions as "correctly unwrapped" in our analysis below.

Figure 10 directly compares the set of correctly unwrapped interferograms and offset tracking displacements, including the nine reference interferograms. For each interferogram time interval, the 2nd and 98th percentiles of the interferometric and offset-tracking displacements rates over the entire landslide are shown (Figure 10a) as well as the displacement rates at three selected locations (Figure 10b). The ranges shown in Figure 10a represent both the noise in the data as well as actual variability in the rates over the entire landslide. Overlap between pairs can be seen in variations of shading. We find a good correlation between interferometric and offset

tracking displacement rates, with offset tracking showing more variability, particularly for short-term pairs, than the interferometric displacement rates.

Figure 10b illustrates the interferogram-derived displacement rates averaged over three selected small areas on the Slumgullion landslide (locations shown in Figure 7). The displacement rates at these three locations possess similar trends but different magnitude.

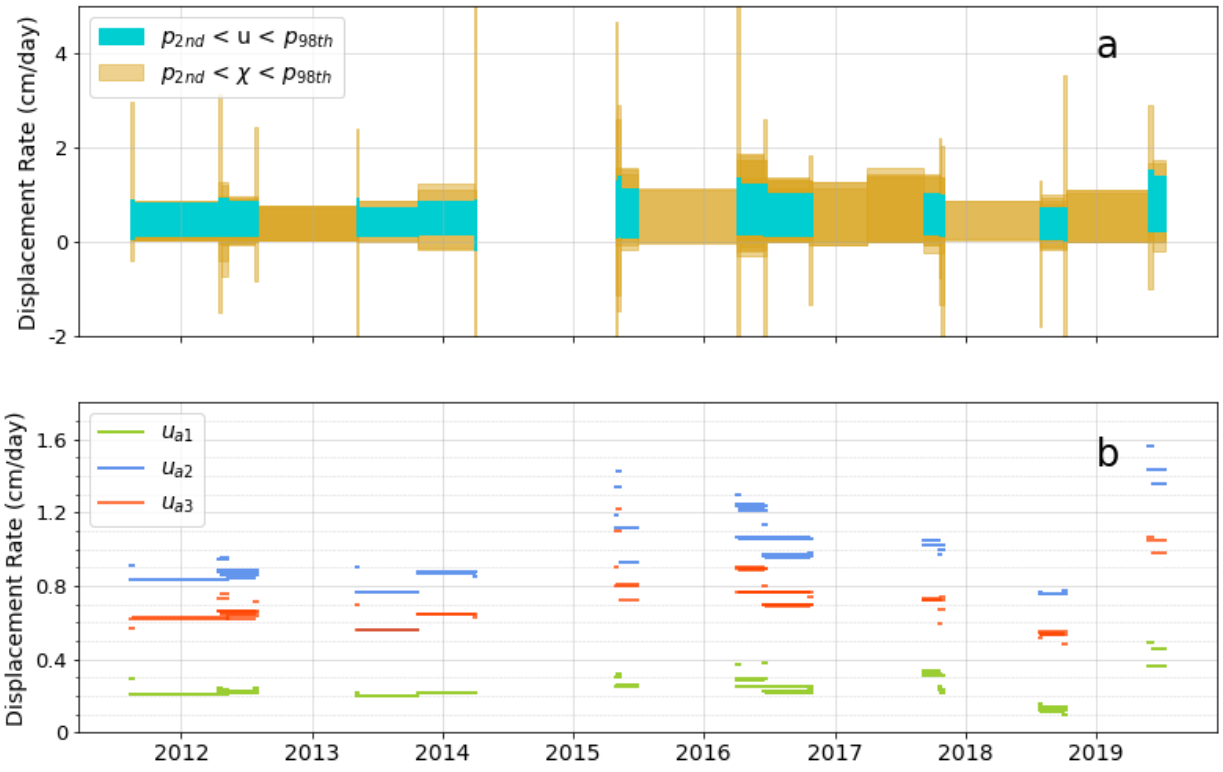

Figure 10. a) The displacement rates (cm/day) from range offset tracking displacements ($\varkappa$) of all seventy-seven image pairs, and for the fifty-four correctly unwrapped interferograms (u). The displacement rates between 2nd percentile (P_{2nd}) and 98th percentile (P_{98th}) over the entire landslide are plotted, in order to represent the spatial variability present in the data. b) The interferogram displacement rates (cm/day, u) for three selected small areas (locations shown in Figure 7, a_1, a_2, and a_3).

One strategy for unwrapping longer-timespan interferograms with low *DPSI* and high *RMSE* values is to use multiple reference interferograms. This can be done by using a reliably unwrapped reference interferogram that is closer in time (and, therefore, less likely to include real variations in displacement rate) to the poor-quality interferogram. We explore this approach for the poor-quality interferograms described above (black circles in Figure 9) by selecting a new reference for each from the set of previously unwrapped interferograms by considering the temporal proximity. The temporal proximity is the average of the absolute time lag between the first images and the absolute time lag between the second images.

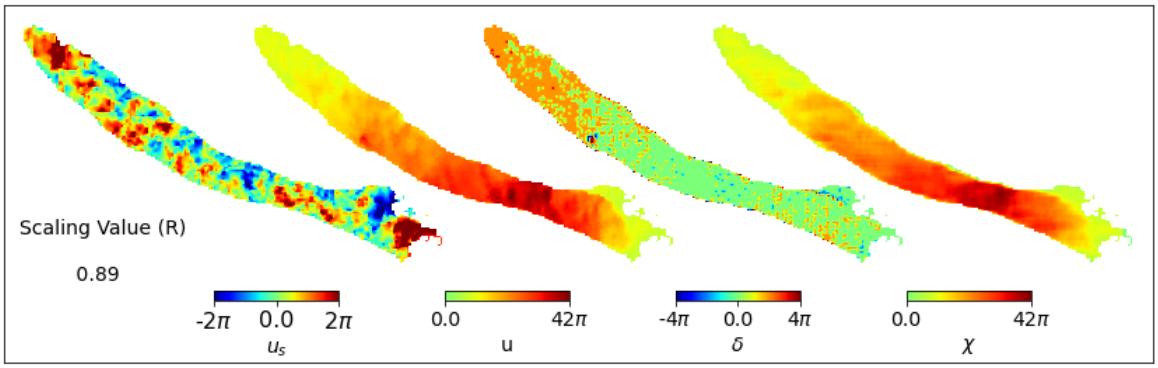

Figure 11. The unwrapped interferogram generated by Snaphu (u_s), the unwrapped interferogram generated by our pattern-based approach using a secondary reference image (u), the difference between the unwrapped interferograms generated using the initial and secondary reference images (δ = secondary unwrapped phase – initial unwrapped phase), and the range direction offset (ϰ) of the pair 2011-08-12 to 2012-05-09. The temporal baseline is 271 days.

This approach decreases the residual phase, increases the DPSI value, and results in a larger number of reliably unwrapped interferograms. In Figure 9, five interferograms, which are circled in red, were initially identified as incorrectly unwrapped interferograms using our initial velocity reference and DPSI and RMSE cutoff values. However, using secondary reference images led to higher DPSI values and smaller RMSE values. Figure 11 illustrates the impact of the use of a secondary reference on one of these five interferograms. The original, much noisier unwrapped interferogram generated by Snaphu (u_s) contrasts greatly with the pattern-based approach (u) using our initial velocity reference, and the range direction offsets (ϰ). We also show the phase difference between the unwrapped interferograms generated using the initial short-baseline reference image and a secondary longer-baseline reference image (δ). The phase difference between the interferograms generated using initial and secondary references is 2π over the tail (upper left, in Figure 11) of the landslide. The phase difference for the rest of the pixels is zero except for small number of pixels where it 4π. The initial DPSI and RMSE values of the interferogram are 0.11, and 1.72. However, the secondary DPSI, and RMSE values are 0.24, and 1.58, respectively.

5. Conclusions

In this paper, we introduce a pattern-based unwrapping method for use in rapidly deforming regions. The approach uses a reference interferogram as an initial pattern of deformation, but allows the overall magnitude of this displacement rates within that reference to vary over time. The residual phase between the unwrapped interferogram using this approach and the scaled, reference interferogram contains any noise or real-world variability between the pattern of deformation used as a reference and the actual deformation occurring within a particular interferogram. We examine the behavior of two metrics, DPSI and RMSE, to characterize the size of the residual phase values. We used a set of synthetic interferograms generated over a small landslide to the southeast of the Slumgullion landslide to examine the impact of noise and temporal variability of strain and find that we reliably unwrap pairs when DPSI is greater than a threshold value of 0.15 and the RMSE is smaller than 1.65. These values would be expected to vary, given the spatial extent, strain rates and noise levels that characterize a given target area.

To evaluate the performance of our approach on real data, and to test how well our quality metrics perform in a different region, we examined UAVSAR interferograms over the Slumgullion landslide in Colorado. The Slumgullion landslide moves with a rate of 1-2 cm/day (e.g., Delbridge et al., 2016; Coe et al., 2003). Therefore, L-band UAVSAR interferograms with temporal baselines larger than seven days are affected by phase aliasing. We examined a total of seventy-seven interferograms, but found that only nine interferograms, all with temporal baselines of seven days or smaller, were reliably unwrapped using the standard workflow. We applied our pattern-based approach to the remaining sixty-eight remaining interferograms and compared the results with the results of range offset tracking. We found that our pattern-based unwrapping method was successful in unwrapping forty-five of the interferograms, and that the interferograms that were reliably unwrapped all had DPSI values larger than 0.15 and RMSE value smaller than 1.65. This result suggests that, even though the Camp Trail landslide differs from the Slumgullion landslide in some respects, the quality metrics derived from the Camp Trail synthetic tests are still applicable to the Slumgullion results, and, perhaps, more widely.

As mentioned previously, over the Slumgullion landslide, UAVSAR interferograms with temporal baselines larger than seven days (and even some interferograms covering shorter timescales) are impacted by aliasing of the phase and present a challenge to traditional unwrapping methods. We found our pattern-based unwrapping approach can unwrap interferograms with displacements of up to about 38 π radians, equivalent to 144 cm, in a manner that agrees well with the independently generated range offset results. We find that the magnitude of inferred displacement varies over time, as expected, and the pattern of deformation within the unwrapped results sometimes has larger or smaller displacement rates in the uppermost or lower regions of the slide.

We also explored the use of a "secondary" reference, where the initial set of longer-timescale interferometric pairs unwrapped using our method could themselves then be used as a reference for more problematic pairs. This allows the use of a reference interferogram that is closer in time to the pair targeted for unwrapping. We find that this approach results in better quality metrics, as expected, with very little change in the actual unwrapped phase. This approach shows promise both as a way to increase the time intervals over which unwrapping can be reliably performed, but also as a means of determining how robust the unwrapping actually is. In the case shown in Figure 11, the final unwrapped phase differs very little when a primary vs. secondary reference is used, suggesting that the result does not depend strongly on the existence of a reference that is temporally close to the target interferogram.

This pattern-based unwrapping approach is simple to implement, somewhat robust to variability in the pattern of deformation, and allows for true variability in the overall rate of deformation within a landslide, as may be expected in locations where rainfall is an important trigger for landslide motion. The approach will not perform well in the presence of vary large amounts of noise, or in cases where the true deformation within an interferogram contains differences in the pattern of strain that are larger than around half of a wavelength. While both of these conditions certainly exist in many areas of interest, our approach can still be used to extend the time periods over which InSAR data can be reliably unwrapped.

Acknowledgments

work was supported by NASA grant NNX16AK57G and 80NSSC19K1496. UAVSAR imagery used in this work was acquired and processed through the support of teams at NASA/JPL-

Caltech and retrieved from the uavsar.jpl.nasa.gov site. Figures were generated using GMT, python and matplotlib.

References

Agram, P. S., Gurrola, E. M., Lavalle, M., Sacco, G. F., & and Rosen, P. A. (2016). The InSAR Scientific Computing Enviroment (ISCE): An Earth Science SAR Processing Framwork, Toolbox, and Foundry. USA.

Bekaert, D. P., Handwerger, A. L., Agram, P., & Kirschbaum, D. B. (2020). InSAR-based detection method for mapping and monitoring slow-moving landslides in remote regions with steep and mountainous terrain: An application to Nepal. *Remote Sensing of Environment, 249*.

Bürgmann, R., Rosen, P., & Fielding, E. (2000). Synthetic aperture radar interferometry to measure Earth's surface topography and its deformation,. *Annu. Rev. Earth Planet. Sci., 28*, 169-209. doi:10.1146/annurev.earth.28.1.169

Carrière, S., Jongmans, D., Chambon, G., Bièvre, G., Lanson, B., Bertello, L., . . . Chambers, J. (2018). Rheological properties of clayey soils originating from flow-like landslides. *Landslides, 15*(8), 1615-1630.

Casu, F., Manconi, A., Pepe, A., & Lanari, R. (2011). Deformation Time-Series Generation in Areas Characterized by Large Displacement Dynamics: The SAR Amplitude Pixel-Offset SBAS Technique. *IEEE Trans. Geosci. Remote Sens., 49*, 2752–2763.

Chen, C. W., & Zebker, H. A. (2002). Phase unwrapping for large SAR interferograms: Statistical segmentation and generalized network models. *IEEE Trans. Geosci. Remote Sens., 40*(8), 1709-1719.

Chen, C. W., & Zebker, H. A. (2011). Two-dimensional phase unwrapping with use of statistical models for cost functions in nonlinear optimization. *J. Opt. Soc. Am. A, 18*, 338-351.

Chen, Y., Wu, P., Yu, Q., & Xu, G. (2017). Effects of Freezing and Thawing Cycle on Mechanical Properties and Stability of Soft Rock Slope. *Advances in Materials Science and Engineering, 2017*. Retrieved from https://doi.org/10.1155/2017/3173659

Coe, J., Ellis, W., Godt, J., Savage, W., Savage, J., Michael, J., . . . Debray, S. (2003). Seasonal movement of the Slumgullion landslide determined from Global Positioning System surveys and field instrumentation, July 1998 - March 2002. *Eng. Geol., 68*, 67-101.

Costantini, M. (1998). A novel phase unwrapping method based on network programming. *IEEE Transactions on Geoscience and Remote Sensing, 36*(3), 813-821. doi:doi: 10.1109/36.673674

Costantini, M., Malvarosa, F., Minati, F., Pietranera, L., & Milillo, G. (2002). A three-dimensional phase unwrapping algorithm for processing of multitemporal SAR interferometric measurements . *Proceedings of IGARSS 2002.* Toronto.

Crosetto, M., Biescas, E., Duro, J., Closa, J., & Arnaud, A. (2008). Generation of advanced ERS and Envisat interferometric SAR products using the sta-ble point network technique. *Photogram. Eng. Remote Sens., 74* (4), 443-450.

Crosetto, M., Monserrat, O., Cuevas-González, M., Devanthéry, N., & Crippa, B. (2016). Persistent Scatterer Interferometry: A review. *ISPRS Journal of Photogrammetry and Remote Sensing, 115*, 78-89. Retrieved from https://doi.org/10.1016/j.isprsjprs.2015.10.011

Delbridge, B. G., Bürgmann, R., Fielding, E., Hensley, S., & Schulz., W. H. (2016). Three-dimensional surface deformation derived from airborne interferometric UAVSAR: Application to the Slumgullion Landslide. *Journal of Geophysical Research: Solid Earth, 121*(5), 3951-3977.

Delbridge, B., Burgmann, R., Fielding, E., Hensley, S., & Schulz, W. (2016). Three-dimensional surface deformation derived from airborne interferometric UAVSAR: Application to the Slumgullion Landslide . *J. Geophys. Res. Solid Earth, 121*, 3951–3977.

Devanthéry, N., Crosetto, M., Monserrat, O., Cuevas-González, M., & Crippa, B. (2014). An approach to persistent scatterer interferometry . *Remote Sens., 6*(7), 6662-6679.

Dias, B. J., & Leitao, N. J. (2002). The ZpiM algorithm: A method for interferometric image reconstruction in SAR/SAS. *IEEE Trans. Image Process., 11*(4), 408–422.

Ebmeier, S. K., Biggs, J., Mather, T. A., & Amelung, F. (2013). Applicability of InSAR to tropical volcanoes: insights from Central America. *Geological Society, London, Special Publications, 380*(1), 15-37.

Ferretti, A., Prati, C., & Rocca, F. (2001). Permanent scatterers in SAR interferometry. *IEEE TGRS, , 39*(1), 8-20.

Flynn, T. J. (1997). Two-dimensional phase unwrapping with minimum weighted discontinuity. *J. Opt. Soc. Amer. A, Opt. Image Sci., vol., 14*(10), 2692–2701.

Fornaro, G., Pauciullo, A., & Reale, D. (2011). A null-space method for the phase unwrapping of multitemporal SAR interferometric stacks. *IEEE TGRS, 49*(6), 2323-2334.

Fried, D. L. (1977). Least-Squares Fitting a Wave-Front Distortion Estimate to an Array of Phase-Difference Measurements. *Journal of the Optical Society of America, 67*, 370-375.

Froude, M., & Petley, D. (2018). Global fatal landslide occurrence from 2004 to 2016. *Nat. Hazards Earth Syst. Sci., 18*, 2161-2181.

Gariano, S., & Guzzetti, F. (2016). Landslides in a changing climate. *Earth Sci. Rev., 162*, 227-252.

Ghiglia, D., & Pritt, M. (1998). *Two-Dimensional Phase Unwrapping: Theory, Algorithms, and Software.* New York: John Wiley and Sons.

Goel, K., & Adam, N. (2014). A distributed scatterer interferometry approach for precision monitoring of known sur-face deformation phenomena. *IEEE TGRS, 52*(9), 5454-5468.

Gomberg, J., Bodin, P., Savage, W., & Jackson, M. (1995). Landslide Faults And Tectonic Faults, Analogs—The Slumgullion Earthflow, Colorado. *Geology , 23*, 41–44.

Handwerger, A., Fielding, E., Huang, M., Bennett, G., Liang, C., & W.H. Schulz. (2019). Widespread initiation, reactivation, and acceleration of landslides in the northern California Coast Ranges due to extreme rainfall. *J. Geophys. Res. Earth Surf., 124*, 1782-1797.

Handwerger, A., Huang, M.-H., Fielding, E., Booth, A., & Bürgmann, R. (2019). A shift from drought to extreme rainfall drives a stable landslide to catastrophic failure. *Sci. Rep., 9*. doi:10.1029/2019JF005035

Hooper, A., & Zebker, H. (2007). Phase unwrapping in three dimensions with application to InSAR time series. *Journal of the Optical Society of America A, 24*(9), 2737-2747.

Hu, X., Bürgmann, R., Fielding, E. J., & Lee, H. (2020). Internal kinematics of the Slumgullion landslide (USA) from high-resolution UAVSAR InSAR data. *Remote Sensing of Environment, 251*. Retrieved from https://doi.org/10.1016/j.rse.2020.112057

Hu, X., Bürgmann, R., Lu, Z., Handwerger, A., Wang, T., & Miao, R. (2019). Mobility, thickness, and hydraulic diffusivity of the slow-moving Monroe landslide in California revealed by L-band satellite radar interferometry. *J. Geophys. Res. Solid Earth, 124*. doi:10.1029/2019JB017560

Huang, M., Fielding, E., Liang, C., Milillo, P., Bekaert, D., Dreger, D., & Salzer, J. (2017). Coseismic deformation and triggered landslides of the 2016 Mw 6.2 amatrice earthquake in Italy. *Geophys. Res. Lett., 44*(3), 1266-1274 .

Itoh, K. (1982). Analysis of the phase unwrapping algorithm. *Appl Opt., 21*(14). doi:10.1364/AO.21.002470

Iverson, R., Reid, M., Iverson, N., LaHusen, R., Logan, M., Mann, J., & Brien, D. (2000). Acute sensitivity of landslide rates to initial soil porosity. *Science, 290 (5491)*, 513-516. doi:10.1126/science.290.5491.513

Kirschbaum, D., & Stanley, T. (2018). Satellite-based assessment of rainfall-triggered landslide hazard for situational awareness. *Earth's Future, 6*, 505-523. doi:10.1002/2017EF000715

Kirschbaum, D., Stanley, T., & Zhou, Y. (2015). Spatial and temporal analysis of a global landslide catalog. *Geomorphology*. doi:10.1016/j.geomorph.2015.03.016

Le Bivic, R., Allemand, P., Quiquerez, A., & Delacourt, C. (2017). Potential and limitation of SPOT-5 ortho-image correlation to investigate the cinematics of landslides: The example of "Mare à Poule d'Eau"(Réunion, France). *Remote Sens. , 9*(106).

Lipman, P. (1976). *Geologic map of the Lake City Caldera area, western San Juan Mountains, southwestern Colorado.* Reston, VA: U.S. Geological Survey. Retrieved from https://doi.org/10.3133/sim3394

Lohman, R. B., & W. D. Barnhart. (2010). Evaluation of earthquake triggering during the 2005-2008 earthquake sequence on Qeshm Island, Iran. *J. Geophys. Res., 115, B12413*. doi:10.1029/2010JB007710

Lu, Z., & Dzurisin, D. (2014). *InSAR Imaging of Aleutian Volcanoes: Monitoring a Volcanic Arc from Space.* Springer Praxis Books, Geophysical Sciences. doi:10.1007/978-3-642-00348-6

Madsen, S., H.A., Z., & J., M. (1993). Topographic mapping using radar interferometry: Processing techniques. *IEEE Trans. Geosci. Remote Sens., 31*(1), 246-256.

Manconi, A. (2021). How phase aliasing limits systematic space-borne DInSAR monitoring and failure forecast of alpine landslides. *Engineering Geology, 287*. Retrieved from https://doi.org/10.1016/j.enggeo.2021.106094

Mohlenbrock, R. (1989). Slumgullion Slide, Colorado. *Nat. Hist. , 98*(9), 34–37.

Molan, Y., Kim, J., Lu, Z., Wylie, B., & Zhu, Z. (2018). Modeling Wildfire-Induced Permafrost Deformation in an Alaskan Boreal Forest Using InSAR Observations. *Remote Sensing, 10*(3). Retrieved from https://doi.org/10.3390/rs10030405

Mora, O., Mallorqui, J., & Broquetas, A. (2003). Linear and nonlinear terrain deformation maps from a reduced set of interferometric SAR images . *IEEE TGRS, 41*(10), 2243-2253.

Oven, K. (2009). Landscape, Livelihoods and Risk: Community Vulnerability to Landslides in Nepal. Durham University.

Pepe, A., & Lanari, R. (2006). On the extension of the minimum cost flow algorithm for phase unwrapping of multitemporal differential SAR interferograms. *IEEE TGRS, 44*(9), 2374-2383.

Pepe, A., Euillades, L., Manunta, M., & Lanari, R. (2011). New advances of the extended minimum cost flow phase unwrapping algorithm for SBAS-DInSAR analysis at full spatial resolution. *IEEE TGRS, 49*(10), 4062-4079.

Perissin, D., & Wang, T. (2012). Repeat-pass SAR interferometry with partially coherent targets. *IEEE TGRS, 50*(1), 271-280.

Qu, F., Lu, Z., Zhang, Q., Bawden, G., Kim, J., Zhao, C., & Qu, W. (2015). Mapping ground deformation over Houston-Galveston, Texas using Multi-temporal InSAR. *Remote Sensing of Environment, 169*, 290-306.

Raspini, F., Ciampalini, A., Del Conte, S., Lombardi, L., Nocentini, M., Gigli, G., . . . Casagli, N. (2015). Exploitation of amplitude and phase of satellite SAR images for landslide mapping: The case of Montescaglioso (South Italy). *Remote Sens., 7*, 14576-14596.

Rosen, P. A., Hensley, S., Zebker, H. A., Webb, F. H., & Fielding, E. J. (1996). Surface deformation and coherence measurements of Kilauea Volcano, Hawaii, from SIR-C radar interferometry. *Journal of Geophysical Research: Planets, 101(E10)*, 23109-23125.

Rosen, P., Hensley, S., Joughin, I., Li, F., Madsen, S., Rodriguez, E., & Goldstein, R. (2000). Synthetic aperture radar interferometry. *Proc. IEEE, , 88*(3), 333-382 .

Schulz, W., & Wang, G. (2014). Residual shear strength variability as a primary control on movement of landslides reactivated by earthquake-induced ground motion: implications for coastal Oregon, US. . *J. Geophys. Res., 119*(7), 1617-1635 .

Scott, C., & Lohman, R. (2016). Sensitivity of earthquake source inversions to atmospheric noise and corrections of InSAR data. *Journal of Geophysical Research: Solid Earth, 121*.

Shi, X., Xu, Q., Zhang, L., Zhao, K., Dong, J., Jiang, H., & Liao, M. (2019). Surface displacements of the Heifangtai terrace in Northwest China measured by X and C-band InSAR observations. *Eng. Geol., 259*. doi:10.1016/j.enggeo.2019.105181

Singleton, A., Li, Z., Hoey, T., & Muller, J. (2014). Evaluating sub-pixel offset techniques as an alternative to D-InSAR for monitoring episodic landslide movements in vegetated terrain. *Remote Sens. Environ., 147*, 133–144.

Sun, L., & Muller, J. (2016). Evaluation of the Use of Sub-Pixel Offset Tracking Techniques to Monitor Landslides in Densely Vegetated Steeply Sloped Areas. *Remote Sens. , 8*(659).

Uieda, L., Tian, D., Leong, W. J., Schlitzer, W., Toney, L., Grund, M., . . . Wessel, P. (2021). PyGMT: A Python interface for the Generic Mapping Tools (Version v0.4.0). Zenodo.

Wang, C., Cai, J., Li, Z., Mao, X., Feng, G., & Wang, Q. (2018). Kinematic parameter inversion of the Slumgullion landslide using the time series offset tracking method with UAVSAR data. *J. Geophys. Res. Solid Earth, 123*, 8110-8124. doi:10.1029/2018JB015701

Wang, T., Shi, Q., Nikkhoo, M., Wei, S., Barbot, S., Dreger, D., . . . Chen, Q. (2018). The rise, collapse, and compaction of Mt. Mantap from the 3 September 2017 North Korean nuclear test. *Science, 361*(6398), 166-170. doi:10.1126/science.aar7230

Wasowski, J., & Bovenga, F. (2014). Investigating landslides and unstable slopes with satellite Multi Temporal Interferometry: current issues and future perspectives. *Eng. Geol., 174*, 103–138. Retrieved from https://doi.org/10.1016/j.enggeo.2014.03.003

Wessel, P., Luis, J., Uieda, L., Scharroo, R., Wobbe, F., Smith, W. H., & Tian, D. (2019). The Generic Mapping Tools (Version 6). *Geochemistry, Geophysics, Geosystems, 20*(11), 5556–5564. Retrieved from https://doi.org/10.1029/2019GC008515

Xu, W., & Cumming, I. (1999). A region-growing algorithm for InSAR phase unwrapping. *IEEE Trans. Geosci. Remote Sens., 37*(1), 124–134.

Yu, H., Lan, Y., Yuan, Z., Xu, J., & Lee, H. (2019). Phase Unwrapping in InSAR : A Review. *IEEE Geoscience and Remote Sensing Magazine, 7*(1), 40-58. doi:10.1109/MGRS.2018.2873644

Yu, H., Xing, M., & Bao, A. (2013). A fast phase unwrapping method for large-scale interferograms. *IEEE Trans. Geosci. Remote Sens.*, *51*(7), 4240–4248.